Large-Eddy Simulation and Subgrid-Scale Modeling

Large-eddy simulation has attracted considerable attention in the recent years. The foundation of this approach is based on the observation that the small-scale turbulence structures are nearly isotropic and quite universal in character while the large-scale structures of turbulent flows vary considerably. In this approach, the small-scale turbulence is modeled through the subgrid-scale stresses while the large eddies are directly calculated.

The averaging process on the grid-scale is outlined in the subsequent section. The basic conservation laws are

Mass

$$\frac{\partial v_i}{\partial x_i} = 0, \tag{1}$$

Linear Momentum

$$\rho\left(\frac{\partial v_i}{\partial t} + v_j \frac{\partial v_i}{\partial x_j}\right) = \frac{\partial t_{ji}}{\partial x_j} + \rho f_i, \tag{2}$$

where v_i is the velocity vector, t_{ji} is the stress tensor and f_i is the body force per unit mass. For a Newtonian fluid

$$t_{ij} = -p\delta_{ij} + \mu\left(v_{i,j} + v_{j,i}\right). \qquad \text{(incompressible)} \tag{3}$$

In large-eddy simulation the flow parameters are decomposed as:

$$v_i = \overline{v_i} + v_i', \quad p = \overline{p} + p', \qquad t_{ij} = \overline{t_{ij}} + t_{ij}', \tag{4}$$

where bar on the top of a letter stands for the large-scale part and a prime denotes the residual (subgrid-scale) part. Following Leonard, the large-scale component of a quantity ϕ is defined as

$$\overline{\phi}(\mathbf{x}) = \int_D G(\mathbf{x}, \mathbf{x}')\phi(\mathbf{x}')d\mathbf{x}', \tag{5}$$

where G is a filtering function and D is the flow domain. A Gaussian filter is frequently used. Note that unlike the traditional Reynolds averaging

$$\overline{\overline{\phi}} \neq \overline{\phi} \quad \text{and} \qquad \overline{\phi'} \neq 0. \tag{6}$$

Applying the filtering procedure to equations (1) and (2), it follows that

$$\frac{\partial \overline{v_i}}{\partial x_i} = 0 \tag{7}$$

$$\rho\left(\frac{\partial \overline{v_i}}{\partial t} + \overline{v_j}\frac{\partial \overline{v_i}}{\partial x_j}\right) = \frac{\partial \overline{t_{ji}}}{\partial x_j} + \frac{\partial t_{ji}^S}{\partial x_j} + \rho f_i\,, \tag{8}$$

where the subgrid-scale stress tensor is defined as

$$t_{ji}^S = -\rho\left(\overline{v_j v_i} - \overline{v_j}\,\overline{v_i}\right) \tag{9}$$

or

$$t_{ji}^S = t_{ji}^R + t_{ji}^L + t_{ji}^C \tag{10}$$

with

$$t_{ji}^R = -\rho\overline{v_j' v_i'}\,, \quad t_{ji}^L = -\rho\left(\overline{\overline{v_j}\,\overline{v_i}} - \overline{v_j}\,\overline{v_i}\right), \tag{11}$$

$$t_{ji}^C = -\rho\left(\overline{\overline{v_j}\,v_i} + \overline{\overline{v_i}\,v_j'}\right). \tag{12}$$

Here t_{ji}^R is the Reynolds stresses, t_{ji}^L is the Leonard stresses and R_{ji}^C is the cross stresses.

The Reynolds stress tensor is commonly modeled by using an eddy viscosity. i.e.,

$$t_{ji}^R = 2\nu_T \overline{D_{ji}}\,, \quad \overline{D_{ji}} = \frac{1}{2}\left(\frac{\partial \overline{v_j}}{\partial x_i} + \frac{\partial \overline{v_i}}{\partial x_j}\right). \tag{13}$$

For eddy viscosity, the Smagorinsky model given by

$$\nu_T = (c_S\Delta)^2\left(\overline{D_{k\ell}}\,\overline{D_{k\ell}}\right)^{\frac{1}{2}}, \tag{14}$$

is frequently used. Here Δ is the size of the grid ($\Delta = (\Delta_1\Delta_2\Delta_3)^{\frac{1}{3}}$), and c_S is the Smagorinsky constant, which is about $c_S \approx 0.21$ (0.17 – 0.24).

The Leonard stresses need not be modeled and may be calculated as part of the solution. The cross stresses was modeled as (Reynolds et al.)

$$t_{ji}^{c} = -\rho c_r \left(\overline{\overline{u}_j \overline{u}_i} - \overline{\overline{u}_j}\,\overline{\overline{u}_i} \right), \tag{15}$$

where $c_r = 1.1$ was originally suggested. Speziale found $c_r = 1$ make the equation Galilean invariant as is required by the Navier-Stokes equation.

Turbulent Channel Flow

Sample results for direct numerical simulation for a turbulent channel flow is presented in this section. Here it is assumed that the flow in the axial and the transverse directions are periodic with period of 660 wall units. The distance between the walls is 250 wall units. The no slip boundary conditions at the surface of the plates at $y^+ = \pm 125$ are imposed. Figure 1 shows the instantaneous velocity vector field at a section across the channel at $t^+ = 200$ and $x^+ = 157.5$. While the vector field is random, the presence of structures near the walls could be clearly seen from this figure.

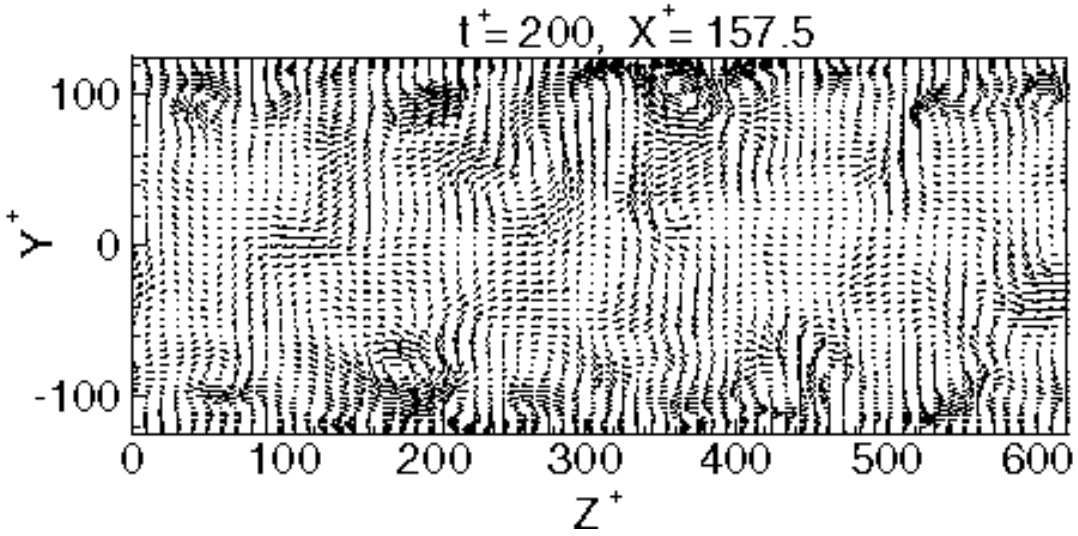

Figure 1. Instantaneous velocity vector field across the channel.

Figure 2a shows another sample instantaneous velocity vector field in the yz-plane at $t^+ = 100$ and $x^+ = 236.25$. While the vector flow varies randomly, it is seen that its general features are similar to those observed in Figure 1. The structures near the wall are still present but are partly shifted and modified. Figure 2b shows the

instantaneous velocity field at a section very close to the lower plate at $y^+ = 3$. This figure shows that near the wall there are roughly periodic high speed and low speed streaks with markedly different velocities.

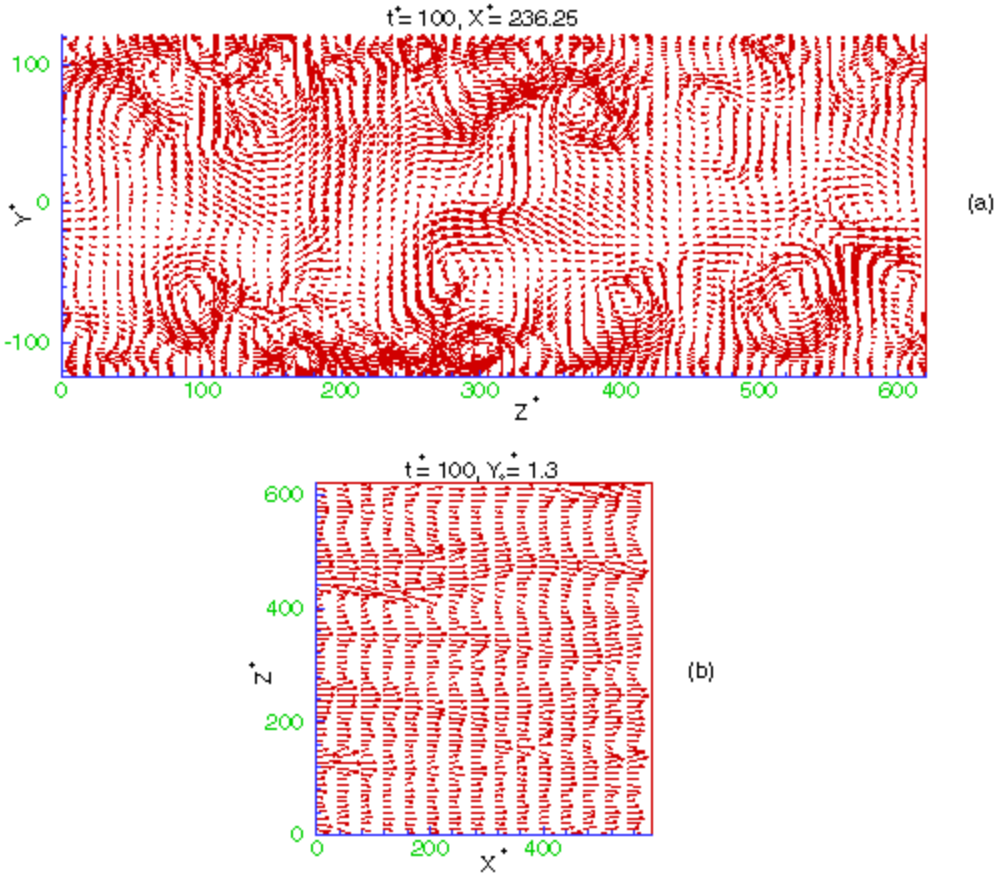

Figure 2. Instantaneous velocity vector field at two planes in the channel.

Figures 3a and 3b, respectively, show the contour plots of short-time mean fluid velocities in the streamwise direction, u^+, and normal to the wall, v^+, in the y-z plane near the upper wall. The short-time mean fluid velocities are obtained by spatial averaging over a distance of 630 wall units in the streamwise direction for a time duration of 100 wall units. Figure 3a shows that the mean streamwise velocity has a roughly periodic variation in the spanwise direction with the distances of nearby high speed (or low speed) regions being about 100 wall units. Similar results for v^+-velocity in Figure 3b shows alternating streams toward and away from the upper wall. Comparing Figures 3a and 3b, it is observed that the locations of high-speed axial streams roughly correspond to the regions that the flow moves toward the wall, and the low-speed axial streams, on the average, coincide with the regions that the flow moves away from the wall.

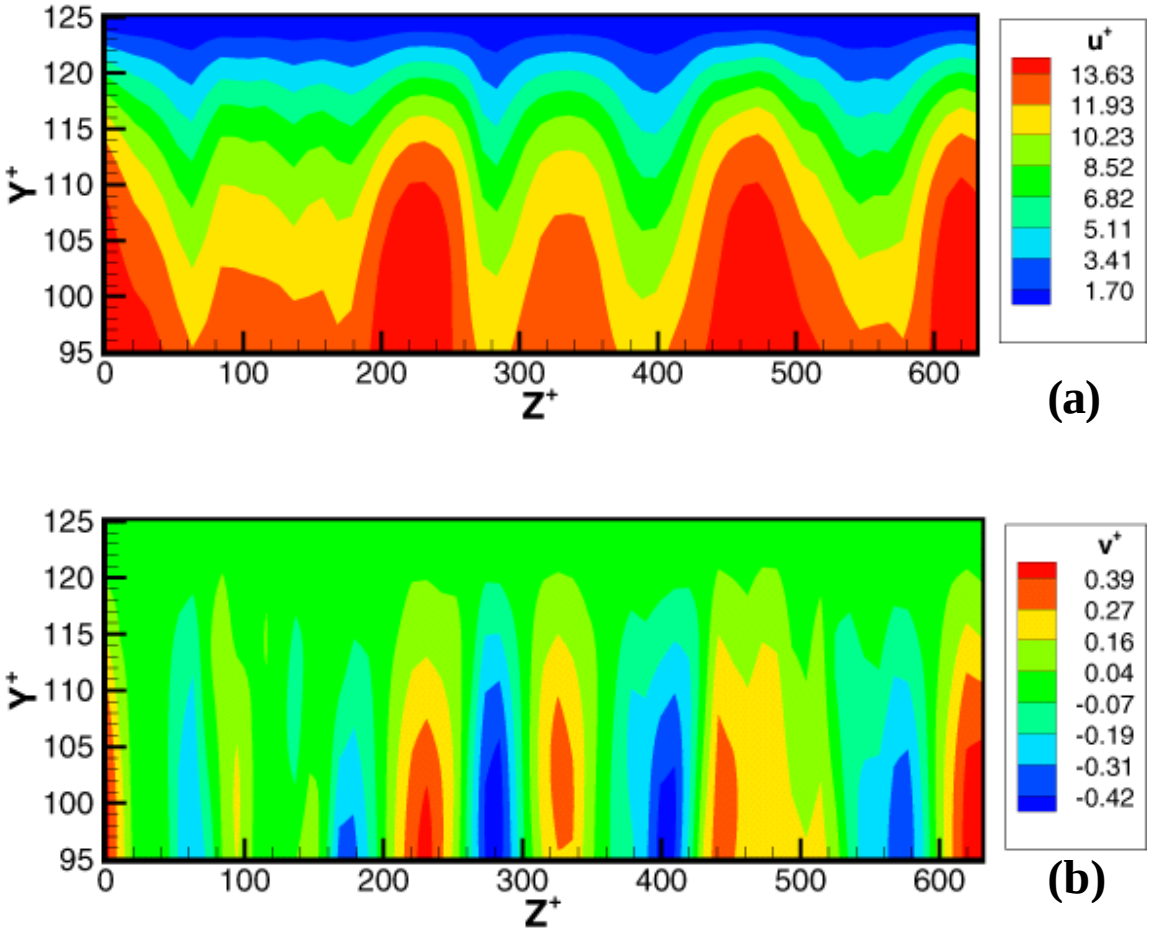

Figure 3. Variations of axial and vertical velocity field near the upper wall.

Figure 4a shows the DNS simulation for different grid resolution and the experimental data of Niederschulte et al. for the mean velocity near the wall. Here, s^+ is the nondimensional distance from the wall. The theoretical linear velocity profile in the viscous sublayer and the logarithmic variations in the inertial sublayer are also shown in this figure for comparison. DNS simulations were performed for grid sizes of $16\times64\times64$, $32\times64\times64$ and $32\times128\times128$. It is observed that the simulated mean velocity is in good agreement with the data and the classical solutions.

The simulated root-mean-square (RMS) fluctuation velocities are shown in Figure 4b and are compared with the earlier high-resolution simulations of Kim et al. Figure 2b shows that the general agreement is reasonable. Figure 2 also shows that the mean velocity and turbulence intensities do not change appreciably when the grid resolution is increased by a factor of 2 to 8.

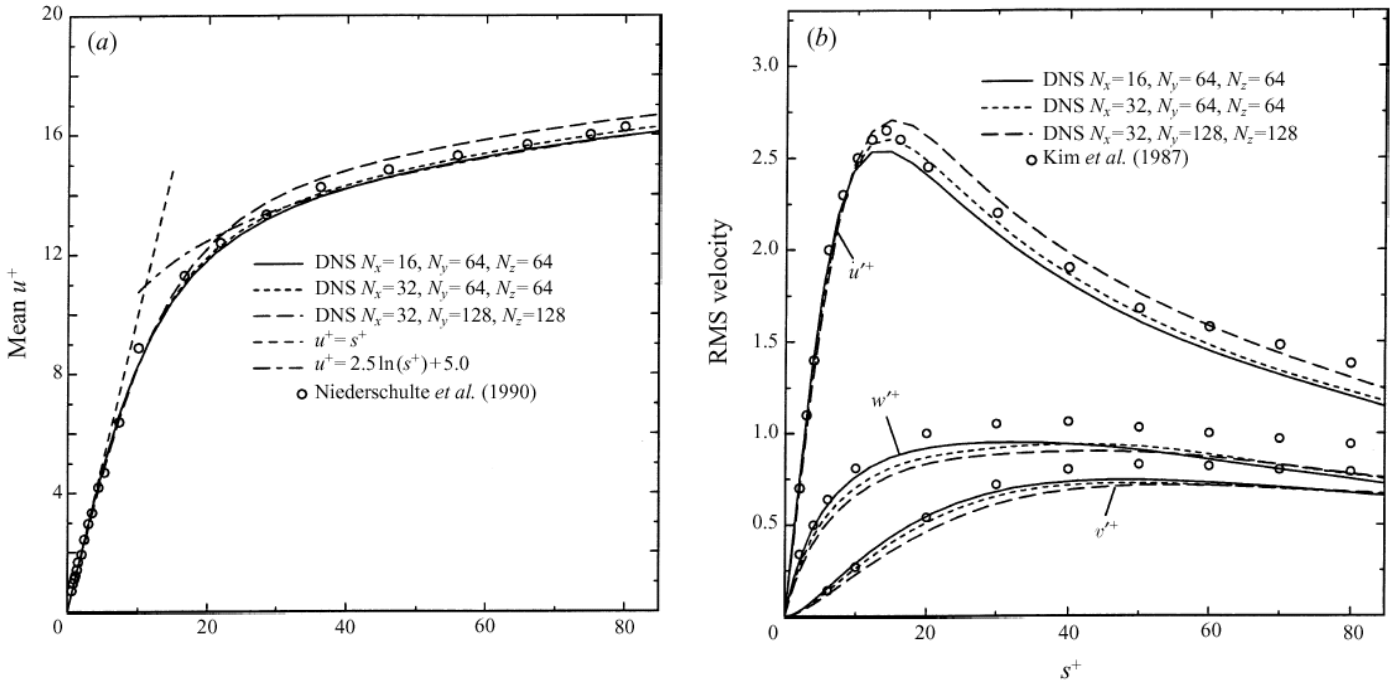

Figure 4. Comparison of the DNS of mean and RMS velocity fields with different grid resolution with the experimental data and earlier simulation results.

Figure 5 shows sample contour plots of a channel flow at high Reynolds number using large eddy simulation (LES). The elongated structure of flow along the flow direction can be clearly seen from this figure.

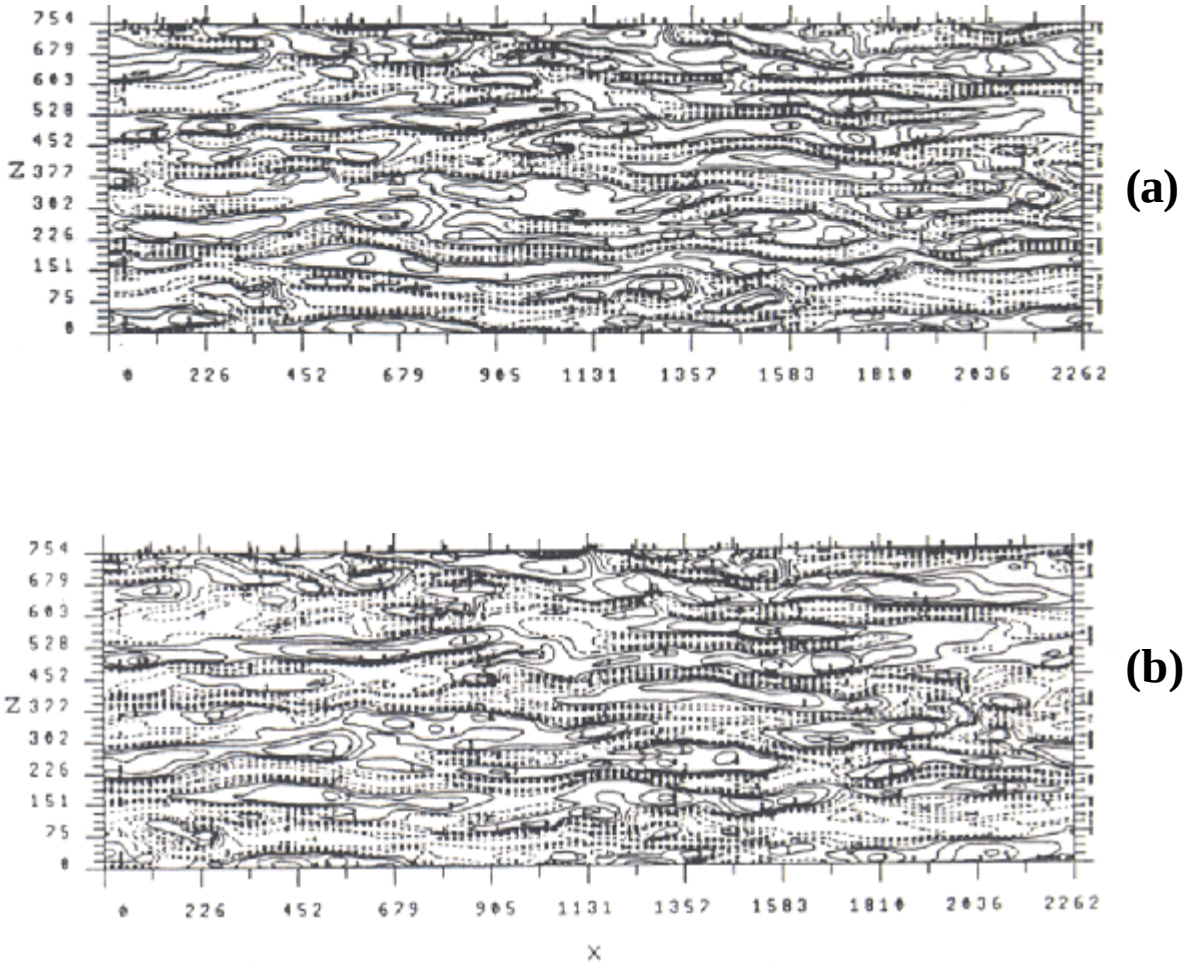

Figure 5. Large eddy simulation (LES) of a turbulent channel flow.